A Barium ($^{138}Ba^{+}$) Optical Clock
A Diagnostic Tool for High Performance Clocks

National University of Singapore

Yeo Wei De Lloyd (A0140473M)

Supervisor: Assoc Prof Murray D. Barrett

Submitted in partial fulfillment of the Requirements

for the

Degree of Bachelor of Science (Hons)

April 5, 2019

Abstract

Barium optical clocks have potential to be used as a sensor to provide accurate calibration of the environment. This capability can be used to determine atomic properties of other species, such as the Lutetium clock that the research group is working on. One application of the Barium clock is in the calibration of laser intensities, which requires determining the differential scalar polarisability, $\Delta\alpha_0(\omega)$ of a Barium $S_{1/2} \leftrightarrow D_{5/2}$ clock transition. Part of the effort to specify $\Delta\alpha_0(\omega)$ involves determining matrix elements $\left\langle P_{1/2}\middle||r|\middle|S_{1/2}\right\rangle$, $\left\langle P_{3/2}\middle||r|\middle|S_{1/2}\right\rangle$ and $\left\langle P_{3/2}\middle||r|\middle|D_{5/2}\right\rangle$. This project is focused on determination of the $P_{1/2} \rightarrow D_{3/2}$ branching ratio, p, one of the quantities needed to specify $\left\langle P_{1/2}\middle||r|\middle|S_{1/2}\right\rangle$. We report the weighted average from $\sim$ 14 billion experiments, $p = 0.267979(21)$, and identify the detector deadtime as a key systematic. Using a measured deadtime $\tau_d = 28.5(2)$ ns, we simulated the deadtime effects and arrived at a preliminary systematic shift of $1 - 2 \times 10^{-4}$ in the branching ratio measurement.

Acknowledgements

I am grateful for the patience and kind assistance of my supervisor, Assoc Prof Murray D. Barrett and research fellow Kyle J. Arnold. I know it must have been tough, frustrating even, to teach a fresh, clueless mind on atomic physics and answering my never ending list of basic, rudimentary questions. I hope I have not been too big of a burden and I am thankful that you guys were so accommodating towards a greenhorn like myself for one whole year. Many times I wished I could have been more competent and capable, so that I can contribute as much as my peers did in their own labs. However, a myriad of personal circumstances and my slow-learning nature resulting in me falling short. But, at the end of the day, I am glad you guys didn't give up on me when it seems like the rest of my world had.

Contents

Chapter 1

Introduction

The advent of the optical atomic clock has brought about greater standards in the measurement of time. This capability is an asset in the modern world. Clocks have helped to push scientific frontiers by contributing to tests of fundamental physics, basic science and precision measurement. They have also played a role in many technological applications, including navigation systems and telecommunications [1]. Thus, it is not surprising to observe consistent efforts at improving clock uncertainty.

In this chapter, a basic background on clocks will be given. Next, we discuss how the Barium ($^{138}Ba^{+}$) clock is used as a sensor to provide support measurements for high performance clocks. Finally, the scope of this project and an outline of this report will be provided.

1.1 Optical atomic clocks

All clocks work on the same basic principle. First, we require a system that exhibits a regular periodic event which provides a stable frequency reference and basic unit of time. Counting cycles of these events produce time intervals. For much of human history, frequency standards were based on celestial observations, e.g. Earth's rotation rate. Then, in the early 20th century came the mechanical clocks using pendulum swings and voltage driven quartz crystal oscillations. Today, the modern atomic clock consists of a laser that is referenced to the resonant frequency of a carefully chosen atomic transition [2].

Optical atomic clocks are at the forefront of timekeeping because they are stable and accurate. Stability is defined as the precision with which we can measure the clock frequency, analogous to how widely scattered a group of arrows fired at a target might be. In general, the stability of an atomic clock, σ_y, can be written as

$$\sigma_y(\tau) \approx \frac{\Delta\nu}{\nu_0\sqrt{N}}\frac{T_c}{\tau}$$

where $\Delta\nu$ is the linewidth of the clock transition, ν_0 as the resonant frequency, N is the number of atoms in each measurement, T_c is the time for a single measurement cycle and τ is the averaging period. The appearance of ν_0 in the denominator implies that it is advantageous to enter the optical domain and run clocks at higher frequency. Alternatively, this can be thought of in terms of line Q, for which optical systems have demonstrated values as high as 10^{15}, five orders of magnitude greater than analogous microwave systems, giving optical clocks a tremendous advantage in terms of frequency stability [1].

Accuracy is defined as how well one can define the frequency, similar to how off center a group of arrows fired at a target might be. This is specified by the determining the systematic effects which shifts the measured frequency from its unperturbed frequency. Examples of such systematics are magnetic field shifts and electric field shifts. In optical clocks, the high stability enables the evaluation of systematic effects more swiftly and precisely, thereby enabling reduced uncertainty budgets [1].

1.2 Role of the Barium clock

Barium is used as a sensor to characterise the environment. There are a few reasons for this choice. First, Barium has well known atomic properties. For example, crucial properties like the g-factors, matrix elements and branching ratios of certain Barium transitions are known to high level of accuracy. These properties are important because they scale the response of Barium towards the environment. Secondly, the Barium clock transition exhibits high sensitivity to the environment. For example, the fractional blackbody radiation shift to the clock transition is on the order 10^{-15} at 300K as opposed to Lutetium's 10^{-18} at the same temperature [3]. A high sensitivity implies a relatively larger response to the environment than other clocks towards the same stimuli. Hence, Barium can be crudely labelled as a 'bad clock' but a good sensor for the environment.

The supporting role of the Barium sensor will be explained further. In clocks, many systematics stem from environmental perturbations. The environment induced shifts to the clock transitions can be broadly described as

$$\text{Shift} \propto \text{Atomic property} \times \text{Environmental factor}$$

Knowledge of both factors is essential for a complete understanding of the shifts in a high performance clock such as Lu^+ clock. Barium's high sensitivity and well-known atomic properties leads to an accurate calibration of environmental factors. Conversely, a well characterised environment can be used to relate well known properties of Barium to corresponding atomic properties in Lutetium.

1.3 Scope

The long term goal is to use Barium to provide accurate calibration of environmental factors, such as magnetic fields, laser intensities. With accurate determination of these quantities, the corresponding atomic property in Lutetium can be better assessed. The calibration of laser intensities involves determining the differential scalar polarisability of a Barium clock transition, which amounts to determining certain relevant matrix elements. One approach enables us to experimentally obtain these matrix elements using just the ac Stark shift, scattering rate and branching ratio measurements. My project is focused on determining the $P_{1/2} \rightarrow D_{3/2}$ branching ratio because it is the most direct experiment to conduct and is manageable within the timeframe of this FYP.

1.4 Outline

The outline for the report will be established here. In chapter 2, a description on Barium and the relevant atomic properties (polarisability and branching ratio) is given. In chapter 3, the experiment set-up and branching ratio measurements are provided. In chapter 4, we identify detector deadtime as a key systematic and assess its effect on our branching ratio estimate. In chapter 5, we briefly discuss other systematics commonly cited in literature but were determined to be insignificant in our experiments. Finally, a summary and future work discussion is provided at the end to conclude this report.

Chapter 2

Barium Ion $^{138}Ba^{+}$

This chapter will first give an introduction to Barium ($^{138}Ba^{+}$) and its level scheme. This is followed by a theoretical discussion on atomic polarisability using perturbation theory. Next, we model the differential dynamic scalar polarisability of the Barium clock transition (for frequencies at and below visible) as a sum of contributions from 3 dominant poles and 1 fictitious pole. We then show a method to determine the matrix element associated with one of the dominant poles using ac Stark shift, scattering rate, and branching ratio experiments (the focus of this project).

2.1 Barium level scheme

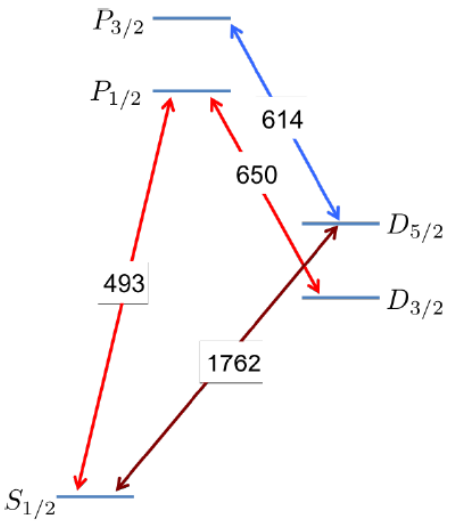

Figure 2.1: Level structure for $^{138}Ba^{+}$ showing clock (brown), detection (red), and repump (blue) transitions. Numbers given are the approximate wavelengths in nm.

The Barium clock transition is the $S_{1/2} \leftrightarrow D_{5/2}$ (1762 nm) transition. The $S_{1/2} \leftrightarrow P_{1/2}$ (493 nm) and $D_{3/2} \leftrightarrow P_{1/2}$ (650 nm) transitions are used in the branching ratio experiment. They also serve a second purpose as Doppler lasers. Doppler cooling is performed on the $S_{1/2} \leftrightarrow P_{1/2}$ transition. The $P_{1/2}$ level has a broad linewidth of 20

MHz, suitable for Doppler cooling, but there is a significant chance of decay to the metastable $D_{3/2}$ state. This level is repumped using 650 nm laser to bring ion back to the cooling state. The 614 nm transition is typically used for repumping when the ion occasionally pumps into the $D_{5/2}$ and becomes dark. However, it is not used in our branching ratio experiments.

2.2 Atomic polarisability

In the presence of an electric field, be it from a laser or blackbody radiation, the energy level of a state will shift. This is known as the Stark effect and the extent of this shift is governed by an atomic property known as the polarisability.

There are two forms of the Stark effect, the dc case and the ac case. We will discuss the simpler dc case first. The interaction Hamiltonian for a field, $\mathcal{E}$, along z-axis,

$$V = -\vec{d} \cdot \vec{\mathcal{E}} = -e\mathcal{E}r_z$$

Since dipole operator is of odd parity, we demand the coupled states to be of different parity. Thus, the first order energy correction vanishes and the second order energy correction of a state $|\gamma, J, m_J\rangle$ is

$$\begin{aligned}\Delta E = \mathcal{E}^2 \sum_{\gamma', J', m'_J} \frac{|\langle \gamma', J', m'_J | r_z | \gamma, J, m_J \rangle|^2}{E_{\gamma,J} - E_{\gamma',J'}} &= \mathcal{E}^2 \sum_{\gamma, J'} \frac{|\langle \gamma', J', m_J | r_z | \gamma, J, m_J \rangle|^2}{E_{\gamma,J} - E_{\gamma',J'}} \\ &= -\frac{1}{2}\alpha_{DC}(\gamma, J, m_J)\mathcal{E}^2\end{aligned}$$

where we used the fact $[r_z, J_z] = 0$ and demanded $\Delta m_J = 0$. And in the last line, we defined the static polarisability of the state $|\gamma, J, m_J\rangle$ as

$$\alpha_{DC} = -2 \sum_{\gamma', J'} \frac{|\langle \gamma', J', m_J | r_z | \gamma, J, m_J \rangle|^2}{E_{\gamma,J} - E_{\gamma',J'}} \tag{2.1}$$

In the ac regime, the perturbation for a z-oriented field now assumes a time dependence

$$V(t) = -\vec{d} \cdot \vec{\mathcal{E}}(t) = -\mathcal{E}_0 r_z \cos(\omega t)$$

The state can be generically written as

$$\Psi(x, t) = \sum_k c_k(t)\psi_k(x)e^{-iE_k t/\hbar}$$

and time-dependent perturbation theory is used to find the probability amplitude, $c_a(t)$,

of a state a. Note that at $t = 0$, $c_k(0) = \delta_{ka}$ because we demand the system to have an initial state $|a\rangle \equiv |\gamma, J, m_J\rangle$. Since the amplitude can be complex,

$$c_a(t) = |c_a(t)|e^{-i\eta(t)}$$

So, the state at some time t,

$$c_a(t)\psi_a(x)e^{-iE_at/\hbar} = |c_a(t)|e^{-i\eta(t)}\psi(x)e^{-iE_at/\hbar} = |c_a(t)|\psi(x)e^{-\frac{i}{\hbar}\int_0^t[E_a+\Delta E_a(t')]dt'}$$

where one can interpret $\Delta E_a(t) = \hbar\dot{\eta}(t)$ as the shift of energy level of state a at time t. The time evolution of a state $|a\rangle$ is

$$U_I\,|a\rangle = \sum_n |n\rangle \underbrace{\langle n|U_I|a\rangle}_{c_n(t)}$$

$$c_n(t) = \delta_{na} + \frac{1}{i\hbar}\int_0^t dt'\,\langle n|V_I(t')|a\rangle + \sum_m \frac{1}{(i\hbar)^2}\int_0^t dt' \int_0^{t'} dt''\,\langle n|V_I(t')|m\rangle\ \langle m|V_I(t'')|a\rangle$$

where V_I is the perturbation in the interaction picture. For $c_a(t)$, the first order correction is zero, leaving the second order correction,

$$c_a(t) = 1 + \frac{1}{(i\hbar)^2}\sum_m \frac{1}{(i\hbar)^2}\int_0^t dt' \int_0^{t'} dt''\left[\,\langle a|V(t')|m\rangle\ \langle m|V(t'')|a\rangle\, e^{i\omega_{am}t'}e^{i\omega_{ma}t''}\right]$$

where $\omega_{ma} = \frac{E_m - E_a}{\hbar} = -\omega_{am}$. Recalling that $c_a(t)$ can be written as $|c_a(t)|e^{-i\eta(t)}$, the time derivative of $c_a(t)$ is

$$\dot{c}_a(t) = \frac{\mathrm{d}|c_a(t)|}{\mathrm{d}t}e^{-i\eta(t)} - ic_a(t)\dot{\eta}(t) \approx -i\dot{\eta}(t)$$

because for small perturbations we expect, $c_a(t)$ to remain close to unity. So the energy shift of a state $|a\rangle$ is related to the time derivative of its probability amplitude,

$$\begin{aligned}\Delta E_a(t) = \hbar\dot{\eta}(t) &= i\hbar\dot{c}_a(t) \\ &= \frac{1}{i\hbar}\sum_{m\neq a}\,\langle a|V(t)|m\rangle\, e^{i\omega_{am}t}\int_0^t dt'\,\langle m|V(t')|a\rangle\, e^{i\omega_{ma}t'}\end{aligned}$$

Defining $\langle a|V(t)|m\rangle = -\mathcal{E}_0\cos(\omega t)\,\langle a|r_z|m\rangle = -\mathcal{E}_0\cos(\omega t)\mu_{am}$, the integration above can be evaluated as

$$\int dt'\,\langle m|V(t')|a\rangle\, e^{i\omega_{ma}t'} = -\frac{\mathcal{E}_0\mu_{ma}}{2}\left(\frac{e^{i(\omega+\omega_{ma})t}-1}{i(\omega+\omega_{ma})} + \frac{e^{-i(\omega-\omega_{ma})t}-1}{-i(\omega-\omega_{ma})}\right)$$

If we plug the above integration result into ΔE_a, and average over time, i.e. $e^{i\omega t} \to 0$,

$$\begin{aligned}\langle \Delta E_a \rangle_t &= -\frac{e^2 \mathcal{E}_0^2}{2\hbar} \sum_{m \neq a} |\langle m|r_z|a\rangle|^2 \frac{\omega_{ma}}{\omega_{ma}^2 - \omega^2} \\ &= -\frac{e^2 \langle \mathcal{E}(t)^2 \rangle_t}{\hbar} \sum_{m \neq a} |\langle m|r_z|a\rangle|^2 \frac{\omega_{ma}}{\omega_{ma}^2 - \omega^2} \\ &= -\frac{1}{2}\alpha(\omega) \left\langle \mathcal{E}(t)^2 \right\rangle_t\end{aligned} \tag{2.2}$$

where the mean squared field $\langle \mathcal{E}(t)^2 \rangle = \frac{\mathcal{E}_0^2}{2}$ and the dynamic polarisability is

$$\alpha(\omega) = \frac{2e^2}{\hbar} \sum_{m \neq a} \frac{|\langle m|r_z|a\rangle|^2}{\omega_{ma}} \frac{1}{1 - (\omega/\omega_{ma})^2} \tag{2.3}$$

A more thorough treatment of the atomic polarisability is given in [4], where the polarisability has a scalar and tensor component. The $\alpha(\omega)$ we found in [2.3] is the scalar component because there is no polarisation dependence and it is the same for all states. Without proof, we state the scalar dynamic polarisability (in atomuc units) of a state from [4],

$$\alpha_0(\omega) = \frac{2}{3(2J_a + 1)} \sum_{m \neq a} \frac{|\langle m||r||a\rangle|^2}{\omega_{ma}} \frac{1}{1 - (\omega/\omega_{ma})^2} \tag{2.4}$$

where J_a is the total angular momentum of state $|a\rangle$, $\langle m||r||a\rangle$ is the reduced matrix element. The above differs from our expression in Eqn (2.3) found by simpler means by a constant.

2.3 Barium dynamic differential scalar polarisability

From computational studies done by the research group, the $\alpha_0(\omega)$ of $S_{1/2}$ state is primarily determined by coupling between $S_{1/2} \leftrightarrow P_{1/2}$ (493 nm) and $S_{1/2} \leftrightarrow P_{3/2}$ (455 nm). The $\alpha_0(\omega)$ of $D_{5/2}$ is primarily determined by coupling between $D_{5/2} \leftrightarrow P_{3/2}$ (614 nm). The rest of the contributions are small and in the UV region.

$$\alpha_0(\omega; S_{1/2}) = \frac{1}{3}\left[\frac{\left|\left\langle P_{1/2}\middle||r|\middle|S_{1/2}\right\rangle\right|^2}{\omega_{493}[1 - (\omega/\omega_{493})^2]} + \frac{\left|\left\langle P_{3/2}\middle||r|\middle|S_{1/2}\right\rangle\right|^2}{\omega_{455}[1 - (\omega/\omega_{455})^2]}\right] + [\text{UV poles}]$$

$$\alpha_0(\omega; D_{5/2}) = \frac{1}{9}\left[\frac{\left|\left\langle P_{3/2}\middle||r|\middle|D_{5/2}\right\rangle\right|^2}{\omega_{614}[1 - (\omega/\omega_{614})^2]}\right] + [\text{UV poles}]$$

We define the differential dynamic scalar polarisability of the clock transition,

$$\Delta\alpha_0(\omega) = \alpha_0(\omega; D_{5/2}) - \alpha_0(\omega, S_{1/2})$$

and this is predominantly determined by three poles at 455, 493, 614 nm. As seen in Figure 2.2, if we focus on frequencies at or below visible ($\omega = 0$ to $\omega = 0.065$ a.u.), the UV poles introduce a dc offset between the theoretical curve (solid line) and the curve generated from 3 poles (dotted line).

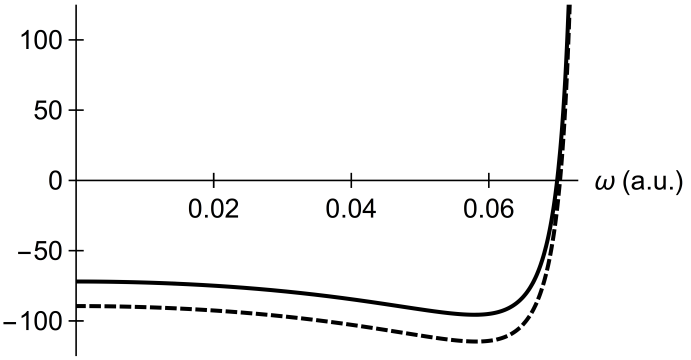

Figure 2.2: Plot of differential dynamic scalar polarisability, $\Delta\alpha_0(\omega)$ against frequency ω in atomic units. The solid curve was obtained from theoretical calculations. The dashed curve is the contribution from the transitions at 455, 493 and 614 nm.

Hence, accurate determination of the matrix elements associated with the three poles and a characterisation of the dc offset should give a reasonably accurate representation of the $\Delta\alpha_0(\omega)$ over the region of interest.

The contribution of the UV poles to the $\Delta\alpha_0(\omega)$ is

$$\begin{aligned}
\sum_{k\subset UV} \frac{C_k}{1-(\omega/\omega_k)^2} &\approx \sum_{k\subset UV} C_k \left(1 + \left(\frac{\omega}{\omega_k}\right)^2 + \left(\frac{\omega}{\omega_k}\right)^4\right) \\
&= C_0 + \left(\frac{\omega}{\omega_1'}\right)^2 + \left(\frac{\omega}{\omega_2'}\right)^4 \\
&= C_0 + C_1\left(\frac{\omega}{\omega_0}\right)^2 + C_1\left(\frac{\omega}{\omega_0}\right)^4 \\
&\approx C_0 + \frac{C_1(\omega/\omega_0)^2}{1-(\omega/\omega_0)^2} \\
&= \frac{C_0}{1-(\omega/\omega_0)^2} + \frac{\overbrace{(C_1 - C_0)}^{\Delta C}(\omega/\omega_0)^2}{1-(\omega/\omega_0)^2}
\end{aligned}$$

where in the second to third line we made the parameterisaton $\omega_1'^2 = \frac{\omega_0^2}{C_1}, \omega_2'^4 = \frac{\omega_0^4}{C_1}$. Using this parameterisation, we can describe the sum of poles as a fictitious pole (C_0 term) and a ΔC term as seen in the final line above. The research group has found that for the $\Delta\alpha_0(\omega)$ of $S_{1/2} \leftrightarrow D_{5/2}$ transition, the ΔC term is negligibly small, so the sum of UV poles can be approximated as a single fictitious pole. With this, the $\Delta\alpha_0(\omega)$ can

well be described by 3 dominant poles and a fictitious pole.

There are certainly errors incurred in such an estimation. However, the research group determined that the maximum error was found to be $\sim 0.5\%$ over the frequencies of interest. This is a desirable level of error because it allows calibration of laser intensities to the same level without any work on the beam characterisation or calibration of the power meter.

2.4 Matrix elements

The contribution from the dominant poles can be determined if the relevant matrix elements are known, $\left\langle P_{1/2}\middle||r|\middle|S_{1/2}\right\rangle$, $\left\langle P_{3/2}\middle||r|\middle|S_{1/2}\right\rangle$ and $\left\langle P_{3/2}\middle||r|\middle|D_{5/2}\right\rangle$. To determine the matrix element $\mu = \left\langle P_{1/2}\middle||r|\middle|S_{1/2}\right\rangle$, we can probe the relevant transition, ω_0 , with a slightly detuned beam $\Delta = \omega - \omega_0$. Thus, $\Delta\alpha_0(\omega)$ would be strongly determined by that pole.

$$\begin{aligned}\Delta\alpha_0(\omega) &\approx -\frac{e^2}{3\hbar}\frac{\mu^2}{\omega_0}\frac{1}{1-(\omega/\omega_0)^2} \\ &= -\frac{e^2\mu^2}{3\hbar}\frac{\omega_0}{\underbrace{(\omega_0-\omega)}_{-\Delta}(\omega_0+\omega)} \\ &\approx \frac{1}{6}\frac{e^2\mu^2}{\hbar\Delta}\end{aligned}$$

where from the second to third line we used $\omega_0 + \omega \approx 2\omega_0$. The ac Stark shift for the clock transition (see Eqn (2.2)) is

$$\Delta E = \hbar\delta f = -\frac{1}{2}\left[\frac{e^2\mu^2}{6\hbar\Delta}\right]\left\langle \mathcal{E}(t)^2\right\rangle_t = -\frac{1}{24}\frac{e^2\mu^2\mathcal{E}_0^2}{\hbar\Delta}$$

$$\Rightarrow \delta f = -\frac{1}{24}\frac{e^2\mu^2\mathcal{E}_0^2}{\hbar^2\Delta} = -\frac{\Omega^2}{24\Delta};\quad \Omega = \frac{e\mu\mathcal{E}_0}{\hbar} \tag{2.5}$$

At the same time, a small detuned beam will lead to considerable scattering out of $S_{1/2}$. Since it is close to resonance, a two level atom approximation ($S_{1/2} \leftrightarrow P_{1/2}$) is valid. The optical Bloch equations for a two level atom at steady state gives the excited state population as

$$\rho_{ee} = \frac{1}{2}\frac{2\Omega^2/\Gamma^2}{1+\frac{2\Omega^2}{\Gamma^2}+\frac{4\Delta^2}{\Gamma^2}} = \frac{1}{2}\frac{s_0}{1+s_0+4\Delta^2/\Gamma^2};\quad s_0 = \frac{2\Omega^2}{\Gamma^2}$$

where Γ is the linewidth of the excited state $P_{1/2}$. In our context, $|\Delta| > \Gamma$ and the saturation is low $s_0 < 1$,

$$\rho_{ee} \approx \frac{s_0}{2}\frac{\Gamma^2}{4\Delta^2} = \frac{\Omega^2}{4\Delta^2}$$

From $P_{1/2}$, the ion can either decay to $D_{3/2}$ with branching ratio p or decay to $S_{1/2}$ with branching ratio $(1-p)$. The scattering rate into $S_{1/2}$ is thus

$$R = (1-p)\Gamma\rho_{ee} = (1-p)\Gamma\frac{\Omega^2}{4\Delta^2} \tag{2.6}$$

Taking ratios of Eqn (2.6) to Eqn (2.5) and rearranging, the overall decay rate out of $P_{1/2}$ can be expressed as

$$\Gamma \propto \frac{R\Delta}{(1-p)\delta f} \propto \left|\left\langle P_{1/2}\middle||r|\middle|S_{1/2}\right\rangle\right|^2 \tag{2.7}$$

Hence, the matrix element of interest can be specified by 4 experimentally determined quantities, (i) scattering rate R, (ii) detuning Δ, (iii) ac Stark shift δf and (iv) branching ratio p.

Chapter 3

Experiment

This chapter opens with the experiment set up and a discussion on the $P_{1/2} \rightarrow D_{3/2}$ branching ratio measurement scheme. Next, it details the results obtained from the branching ratio measurements.

3.1 Experiment setup

$^{138}Ba^{+}$ ions are produced by photo-ionisation of Barium. A single $^{138}Ba^{+}$ ion is loaded into a linear Paul trap and illuminated by the 493 nm and 650 nm beams. With reference to Figure 3.1, we define a coordinate frame to specify the orientations of various components of the experiment. The 493 nm and 650 nm beams co-propagate in the z direction. The 493 nm beam and 650 nm beam are linearly polarised in the x and y directions respectively. The Single Photon Counting Module (SPCM) detector (Perkin Elmer SPCM-AQR-16) is located along the x axis.

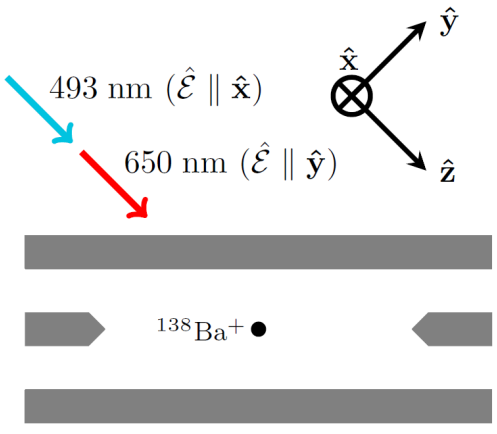

Figure 3.1: Experiment setup relative to a specified coordinate frame.

The fluorescence from the ion is collected using an aspheric lens with numerical aperture (NA) of 0.42, imaged through a 650 nm narrow-band filter onto the SPCM

with reported quantum efficiency of 65%. The efficiency of the aspheric lens is

$$\frac{1}{4\pi}\int_0^{\theta/2} d\theta \sin\theta \int_0^{2\pi} d\phi = 0.046$$

where $\theta/2 = \sin^{-1}(\text{NA})$. This gives an estimate of the detection efficiency at 3%. Our experiments yielded a detection efficiency $\approx 2.7\%$, which is consistent to within 10% of the NA and quantum efficiency specifications.

3.2 Branching ratio

Before each experiment, we conducted measurements of the optical pumping times, τ, for the 493 nm (pumps $S_{1/2} \rightarrow D_{3/2}$) and 650 nm beams (pumps $D_{3/2} \rightarrow S_{1/2}$). τ can be interpreted as the characteristic time scale over which the population of the initial state exponentially decays into the target state.

3.2.1 Measurement scheme

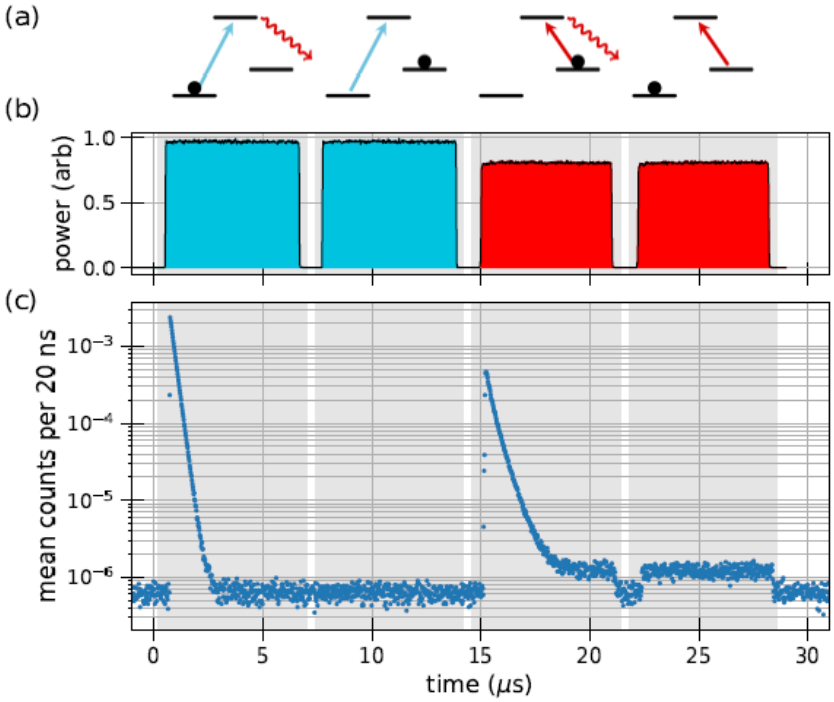

Figure 3.2: (a)Sequence of pumping pulses. (b) Measured intensity profiles of 493 nm (blue) and 650 nm (red) laser pulses. (c) Example of measured signals from 4.9×10^7 experiments using high resolution time tagging (0.25 ns). The detection events within the grey region are accumulated to obtain the four signals, $b, \bar{b}, r, \bar{r}$.

With reference to Figure 3.2, we describe the the experiment scheme to determine the branching ratio of $P_{1/2} \rightarrow D_{3/2}$.

1. Pump ion from $S_{1/2}$ to $D_{3/2}$ with 493 nm for duration T. This will step will ideally emit one photon and is collected with a detection efficiency, q.
2. Measure background counts with 493 nm turned on for duration T.
3. Pump ion from $D_{3/2}$ to $S_{1/2}$ using 650 nm for duration τ. On average, the ion will emit $\frac{p}{1-p}$ photons, of which $\frac{qp}{1-p}$ gets detected.
4. Measure background counts with 650 nm turned on for duration T.
5. The above 4 steps constitute one cycle. The T here is normally 6μs. Accounting for small delays between each pulse, a single cycle spans about 31 μs.
6. Every 10^4 cycles (defined as one experiment block), there is approximately 44 ms of Doppler cooling where the 493 and 650 nm beams are on.

We introduce the following notation that will be used for this report.

Notation	Intepretation
b	Mean number of red photons collected when pumping ion from $S_{1/2}$ to $D_{3/2}$ from N experiment cycles.
$\bar{b}$	Mean number of red photons collected during background measurement with 493 nm on, from N experiment cycles.
r	Mean number of red photons collected when pumping ion from $D_{3/2}$ to $S_{1/2}$ from N experiment cycles
$\bar{r}$	Mean number of red photons collected during background measurement with 650 nm on, from N experiment cycles.

Table 3.1: Description of notation to be used in this report.

Based on the above table, the detection efficiency q, is

$$q = b - \bar{b} \tag{3.1}$$

After accounting for background, the mean number of photons collected when pumping the ion from $D_{3/2}$ to $S_{1/2}$ is

$$s = r - \bar{r} = \frac{qp}{1-p} \tag{3.2}$$

The branching ratio p is estimated via

$$\bar{p} = \frac{s}{s+q} = \frac{r-\bar{r}}{b+\bar{b}+r-\bar{r}} \tag{3.3}$$

3.2.2 Pre-measurement calculations

It is worthwhile to assess the effort needed to experimentally determine $\bar{p}$ to the desired level of uncertainty. To simplify the analysis, we ignore background noise.

$$\begin{aligned}(d\bar{p}) &= \sqrt{\left(\frac{\partial\bar{p}}{\partial s}\right)^2(ds)^2 + \left(\frac{\partial\bar{p}}{\partial q}\right)^2(dq)^2} \\ &= \bar{p}(1-\bar{p})\sqrt{\left(\frac{ds}{s}\right)^2 + \left(\frac{dq}{q}\right)^2}\end{aligned} \tag{3.4}$$

In pumping the atom from $S_{1/2}$ to $D_{3/2}$ exactly one photon is emitted. The probability of its detection is described by the Bernoulli trial,

$$b(x;q) = \begin{cases}(1-q) & x=0 \\ q & x=1 \\ 0 & \text{otherwise}\end{cases}$$

The variance of this distribution is $q(1-q)$. For N experiments, and using Central Limit Theorem, the sample standard deviation is $\sqrt{\frac{q(1-q)}{N}}$. Thus,

$$\frac{dq}{q} = \sqrt{\frac{1-q}{Nq}} \tag{3.5}$$

When pumping ion from $D_{3/2}$ to $S_{1/2}$, the ion emits n photons according to a geometric distribution.

$$G(n;p) = p^n(1-p)$$

Out of n photons emitted, $k \leq n$ of them are detected and they are governed by a binomial distribution

$$B(k;n,q) = \binom{n}{k} q^k(1-q)^{n-k}$$

The effective distribution for detected photons is simply a joint probability distribution comprising of a geometric and binomial distribution

$$f(k;p,q) = \sum_{n=k}^{\infty} G(n;p)B(k;n,q) = \frac{(1-p)p^kq^k}{(1-p(1-q))^{k+1}} \tag{3.6}$$

where the second equality can be generated from Mathematica. The mean of this distribution is

$$\sum_k f(k;p,q)k = \frac{pq}{1-p} = s \tag{3.7}$$

which exactly matches Eqn (3.2). The variance of $f(k;p,q)$ is $s^2(\frac{1-p+pq}{pq})$. So,

$$\frac{ds}{s} = \sqrt{\frac{1-p+pq}{Npq}} \tag{3.8}$$

Plugging Eqn (3.5) and (3.8) into Eqn (3.4), the fractional error for our branching ratio estimate is

$$\frac{d\bar{p}}{\bar{p}} = \frac{1-p}{\sqrt{Npq}} \tag{3.9}$$

This error is solely statistical in nature, and completely neglects background noise (which tends to contribute to the error). However, it gives a sense of how many N experiments we need to conduct to get to the desired level of accuracy. Using expected values of $p = 0.268$, $q = 0.0268$, and $N = 10^9$, the fractional error is $\sim 3 \times 10^{-4}$. In light of this, a typical run has $\sim 10^9$ experiments.

Aside from the statistical error in our estimate, it is also important to check for the error associated with estimation bias due to non-linearity of the equation,

$$\bar{p} = \frac{s}{s+q} = \frac{1}{1+(q/s)} = \frac{1}{1+x}; \qquad x = \frac{q}{s}$$

If we perform a taylor expansion of the branching ratio estimate, $\bar{p}$, at $\langle x \rangle$,

$$\bar{p} \approx \frac{1}{1+\langle x\rangle} - \frac{(x-\langle x\rangle)}{(1+\langle x\rangle)^2} + \frac{(x-\langle x\rangle)^2}{(1+\langle x\rangle)^3}; \qquad \langle x\rangle = \frac{1-p}{p}$$

If we average the above equation, $(x - \langle x\rangle)$ averages to zero and $(x - \langle x\rangle)^2$ gives the statistical uncertainty in x, denoted as σ_x. Consequently,

$$\bar{p} \approx p(1 + p^2\sigma_x^2)$$

Using Eqn 3.5 and 3.8, σ_x can be written as

$$\sigma_x = \frac{1}{\sqrt{Npq}}$$

and the fractional error in our estimation of the branching ratio due to estimation bias

$$p^2\sigma_x^2 = \frac{p}{Nq}$$

In our experiments, we anticipate $p/q \sim 10$ and $N \sim 10^9$, so this effect is dominated by the statistical uncertainty and is negligible at the level of precision we are interested in.

3.2.3 Experiment results

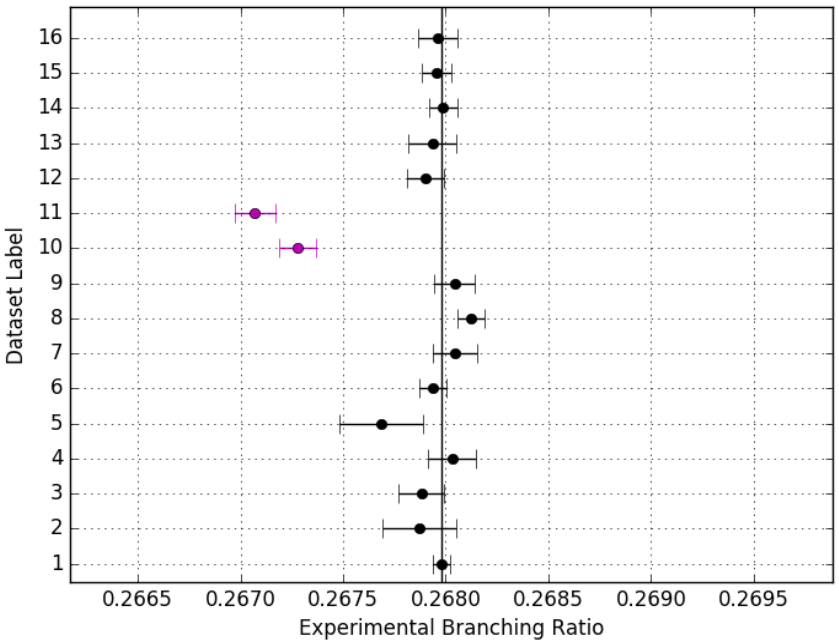

Figure 3.3: (dots) Raw measurements of branching ratio using Eqn (3.3). (dots) Raw measurements of branching ratio with weighted mean (black line) of $p = 0.267979(21)$ excluding outliers (purple dots).

Figure 3.3 shows the branching ratio measurements, $\bar{p}$ from 16 runs (dots), with their associated statistical error. The pumping times for the 493 nm and 650 nm beams were measured for each dataset and they were sufficiently fast such that negligible population ($< 10^{-7}$) is not optically pumped by the end of the pulse (typically 6μs). Excluding the two outlier points (purple dot), we compute the weighted mean of the black dots. This can be done by a χ^2 minimisation,

$$\chi^2(p) = \sum_i^n \left(\frac{(\bar{p}_i - p)}{\sigma_i} \right)^2$$

where p is the weighted mean, $\bar{p}_i$ is the branching ratio measurement of the ith run, and

σ_i is its associated statistical uncertainty. Minimising χ^2 yields p as a function of p_i.

$$\frac{\mathrm{d}\chi^2(p)}{\mathrm{d}p} = 0 \Rightarrow p = \frac{\sum \frac{p_i}{\sigma_i^2}}{\sum \frac{1}{\sigma_i^2}} = f(p_i)$$

The uncertainty in p is

$$(\Delta p)^2 = \sum_i^n \left(\frac{\partial f(p_i)}{\partial p_i}\right)^2 \sigma_i^2 \Rightarrow \Delta p = 21 \times 10^{-6}$$

The preliminary value of the branching ratio (from taking weighted average of raw measurements) is

$$p = 0.267979(21) \tag{3.10}$$

with reduced $\chi^2_\nu = 0.79$ and a fractional uncertainty of 8×10^{-5}.

Also, we have identified two key systematics that have a statistically significant effect on the branching ratio measurements. The first systematic is the detector deadtime. This suppresses the counts that we receive from the ion, especially when pumping from $D_{3/2}$ to $S_{1/2}$. Using Eqn (3.3), this results in an underestimate of p. The detailed description of this systematic will be dealt with in the next chapter. The second systematic is the imperfect background subtraction. There was a small but statistically significant difference ($\sim 1\%$) between the background levels of the first and second red pulses, and this has to be taken into account in the branching ratio estimate. Presently, we are working to assess these effects and we expect the final fractional uncertainty to be $\sim 1 - 2 \times 10^{-4}$.

3.2.4 Statistical limitation of measurements

In the above section, it was stated that all measurements, $b, \bar{b}, r, \bar{r}, \bar{p}$ are statistically limited. Ideally, photon emissions from the ion are governed by Poisson statistics, so given a rate R, the counts measured over time T is $C = RT \pm \sqrt{C}$. The fractional uncertainty in the counts, $\frac{1}{\sqrt{C}} = \frac{1}{\sqrt{RT}}$, is a function of the measurement time. Thus, by averaging over longer periods the fractional uncertainty decreases, and a measurement is statistically limited if its fractional Allan deviation has the same behaviour. The Allan deviation σ_a, is a function of averaging time τ,

$$\sigma_A(\tau) = \frac{1}{2(N-1)} \sum_{i=1}^{N} (\bar{y}_\tau(i+1) - \bar{y}_\tau(i))^2 \tag{3.11}$$

where the measurements are partitioned into N bins of length τ, and $\bar{y}_\tau(i)$ is the average value of the ith bin.

For the s and q measurements, we plot the fractional Allan deviation and the statistical uncertainty with respect to averaging time in Figure 3.4. For the duration of runs ($\sim 10^5$ experiment blocks), the s and q measurements used in Eqn (3.3) are statistically limited over the experiments that were conducted. Since the branching ratio estimate,

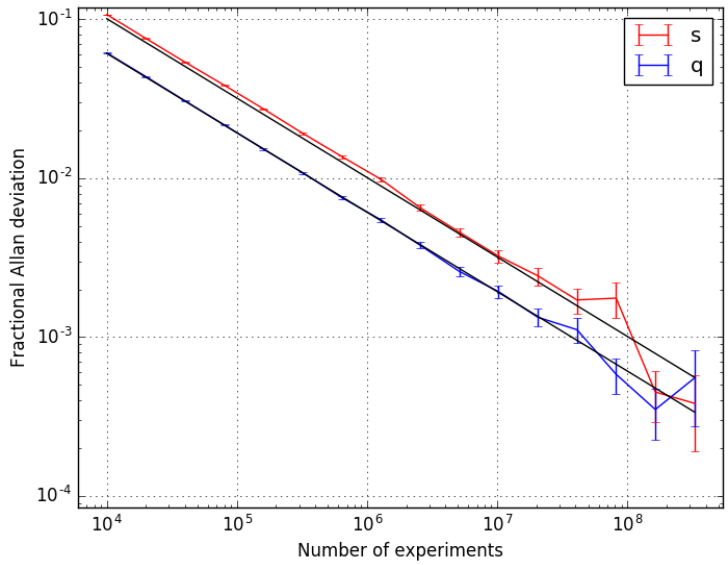

Figure 3.4: Plot of fractional Allan deviation for s (red) and q (blue) measurements against number of experiments. The black lines are the statistical limit associated with s and q

$\bar{p}$, is derived from s, q, it is also statistically limited over the number of experiments that were conducted, as seen in Figure 3.5.

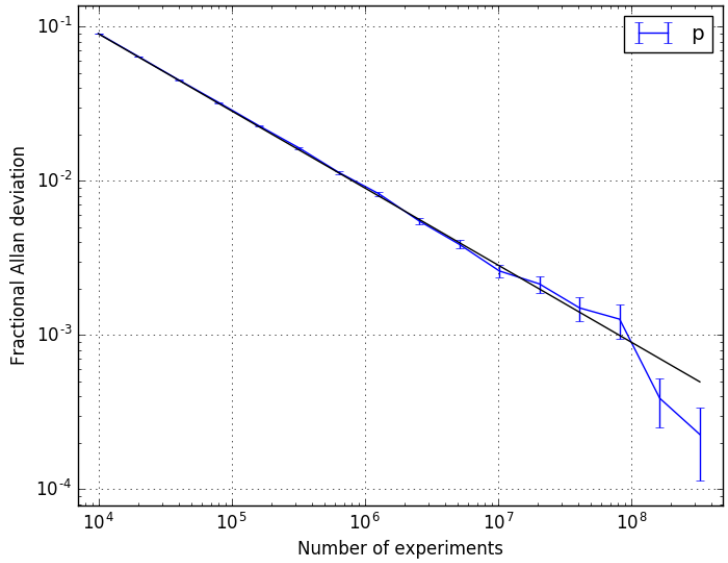

Figure 3.5: Plot of fractional Allan deviation for branching ratio estimate $\bar{p}$ against number of experiments. The black line indicates the statistical limit for $\bar{p}$.

Chapter 4

Key Systematics: Detector deadtime

In this chapter, we first describe the attempts to experimentally measure the detector deadtime. Next, we demonstrate various models to correct for deadtime effects in the branching ratio estimate.

4.1 Background

The deadtime in SPCM is a consequence of its working mechanism. When a photon comes in, an electron hole pair is created and a strong reverse bias voltage triggers an avalanche breakdown. When this occurs, the current rises and rapidly reaches a steady-state value. This is stopped by a quenching circuit which reduces the bias voltage below breakdown. Until this bias is restored, there is a time window during which the SPCM is non responsive to incoming photons and no counts are registered [5]. In our experiments, this would reduce the count rate depending on the photon arrival statistics and distort the branching ratio measurement.

Aside from deadtime, there is a secondary effect at work, known as afterpulsing. This is a small probability in generating a secondary pulse following a detection event. Briefly speaking, during the avalanche, some carriers can be trapped in deep levels of the semiconductor band structure and released at a later time after the bias is restored [6]. Thus, afterpulses are restricted to the occurring after the deadtime of the detection event. Overall, the afterpulsing effect is expected to provide a fractional increase on the mean counts, which cancels out in the branching ratio estimate.

4.2 Deadtime measurement

The first step to assessing a deadtime effect is to measure the detector deadtime. We attempted to determine the deadtime via two methods.

4.2.1 Method 1: Count rate vs. power

This method attempts to indirectly determine the detector deadtime by measuring the power of the beam before entering the detector and the counts that the detector record. A stabilised laser was split into two. The first beam goes to a power meter. The second beam was attenuated and directed into the SPCM. If the second beam going into the SPCM has a rate of λ, the rate n detected by the SPCM is [7],

$$n = \frac{\lambda}{1 + \lambda\tau_d} = \frac{\alpha P}{1 + \alpha P \tau_d} \tag{4.1}$$

where τ_d is the deadtime, P is the power we measure in the first beam, α is a scale factor that relates λ and P. In Figure 4.1, we fitted the data (red dots) to the model (Eqn (4.1) and obtained the fitting curve (blue line) with $\tau_d = 33.7$ ns and $\alpha = 3.28 \times 10^5$ as fit parameters. Upon plotting the fractional difference between the fit and the data points in Figure 4.2, it is clear that there is some systematic variation of the residuals, indicating that the model is a poor fit. Furthermore, $\tau_d = 33.7$ ns is in large disagreement with the manufacturer specified deadtime of ~ 28 ns.

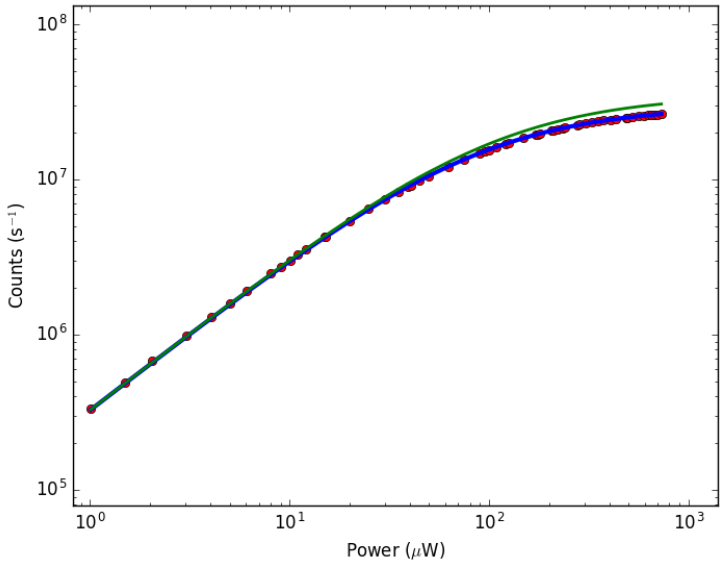

Figure 4.1: Plot (red dots) of counts observed against the power applied with the fitting curve (blue line). The green line is a plot of Eqn (4.1) using $\tau_d = 28$ ns, further implying that Eqn (4.1) may not be a good fitting model

4.2.2 Method 2: High resolution time tagging

Since the indirect method does not fit well with the data, we were motivated to attempt a direct measurement of the deadtime. We direct a beam ($\sim$ 76 cts/s) to a high resolution time tagging module (2 ns resolution) and obtained the arrival times of

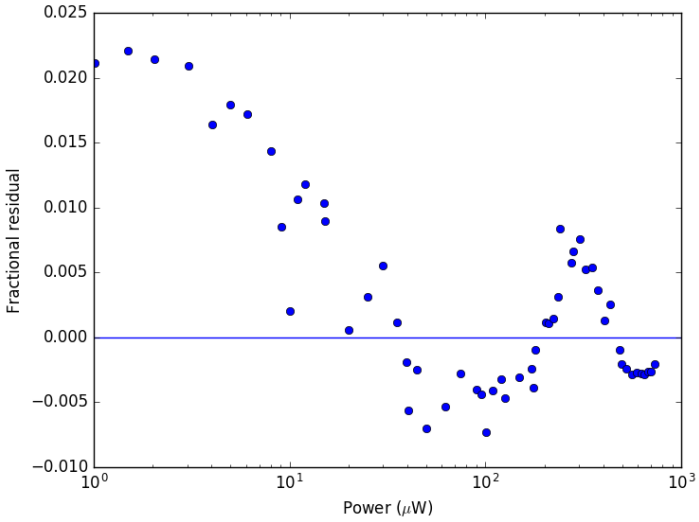

Figure 4.2: Plot of the fractional difference between the fit and the datapoints.

the photons. As expected, the interarrival times between photons are well captured by an exponential fit, shown in Figure 4.3.

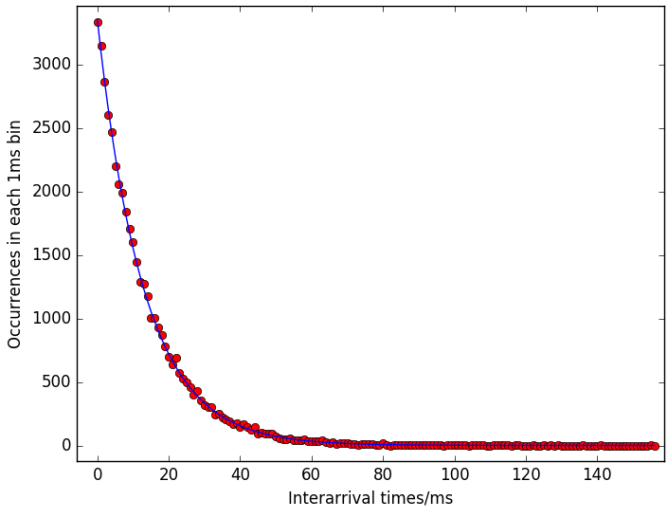

Figure 4.3: Histogram (red dots) of the occurrences in each interarrival time bin (1ms) and the exponential fit (blue).

In Figure 4.4, we zoom in to interarrival times below 200 ns. One can observe the minimum interarrival time between photons at 28(2) ns. This is a direct indication of the detector deadtime because this is the shortest time between detection events. Another feature of interest is the discrepancy between the observed occurrences (red dots) and the exponential fit predicted occurrence (blue line). This is attributed to afterpulsing and we deduce an afterpulsing probability of $\sim 0.36\%$.

After this initial measurement, we repeat the above procedure for beams of various intensities using time taggers with higher resolution. It was found that the deadtime measured varied from 28.5 ns (at low saturation; 170 kcts/s) to about 33 ns (at high

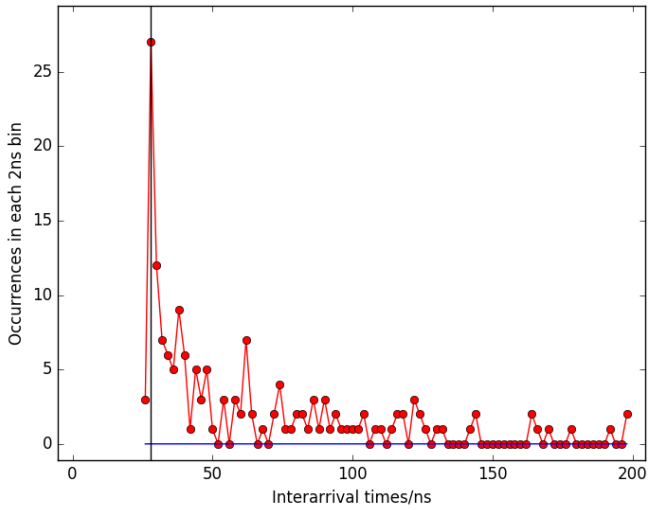

Figure 4.4: Histogram (red dots) of the occurrences in each time bin (2 ns) and the expected occurence in each bin from the exponential fit (blue)

saturation; 20 Mcts/s). This would explain why the previous method fail because it assumes a constant deadtime. For our branching ratio experiments, a low saturation regime holds and we use a deadtime of 28.5$\pm$2 ns for assessing systematic shifts.

4.3 Deadtime corrections

We examine the four measurements, $b, \bar{b}, r, \bar{r}$ and consider in which measurement deadtime effects manifest. Firstly, the background measurements $\bar{b}$ and $\bar{r}$ are small to begin with, and the probability of getting two photons is on the order 10^{-6}, thus we safely neglect deadtime effects here. Secondly, pumping the ion from $S_{1/2}$ to $D_{3/2}$ results in only one photon emitted, so deadtime cannot manifest here. Thus, we only consider deadtime effects on r because pumping the ion from $D_{3/2}$ to $S_{1/2}$ may result in multiple photons emitted.

From here, we present the methods used to assess the deadtime effects, in increasing order of complexity. We start with a model that has a simplistic assumption of population dynamics and a basic rate correction to account for deadtime. Then we add a new layer of complexity that accounts for the quantum nature of the population dynamics. Finally, we consider the photon emission time statistics, $P(t)$, from the master equation and use it to estimate the probability of subsequent photons coming in within the deadtime of the detection event.

4.3.1 Rate equation population dynamics with rate correction

This model was motivated by the desire to assess the deadtime effects in a simple and less computationally intensive manner. While it is not the most comprehensive model,

it offers a sense of the branching ratio corrections to reasonable degree.

The population dynamics is simulated as follows. Assuming a constant pulse, the rate at which the ion pumps out of $D_{3/2}$ into $P_{1/2}$ is related to the $D_{3/2} \rightarrow S_{1/2}$ pumping times τ via

$$R = \frac{1}{\tau(1-p)} \tag{4.2}$$

Defining variables $g(t), e(t), m(t)$ to be the time dependent population of $D_{3/2}$, $P_{1/2}$ and $S_{1/2}$ state, Γ to be the decay rate of $P_{1/2}$, and choosing the best known estimate of $p = 0.268, q = 0.0268$, the rate equations are

$$\begin{aligned} \frac{\mathrm{d}g}{\mathrm{d}t} &= -Rg + \Gamma pe \\ \frac{\mathrm{d}e}{\mathrm{d}t} &= -\Gamma e + Rg \\ \frac{\mathrm{d}m}{\mathrm{d}t} &= \Gamma(1-p)e \end{aligned} \tag{4.3}$$

It should be noted that these equations do not account for the internal 'switch on' time of the atom. In reality, an atom can only emit a photon after it is excited to the upper state. The above equations were then solved with the initial conditions $g = 1, e = 0, m = 0$. Using the time dependent population of the excited state, $e(t)$, the rate of emission of red photons is

$$\lambda(t) = qp\Gamma e(t) \tag{4.4}$$

This construction of $\lambda(t)$ is such that the integral over the pulse time gives the ideal mean red photons emitted

$$\int \lambda(t)dt = \frac{qp}{1-p}$$

The corrected rate, $\lambda_c(t)$, due to detector deadtime, τ_d, [7] is

$$\lambda_c(t) = \frac{\lambda(t)}{1 + \tau_d\lambda(t)} \tag{4.5}$$

The measured red photon counts is computed by taking the time integral of $\lambda_c(t)$ over the full pulse duration. With this we can compute the new branching ratio estimates under an ideal (constant) pulse. (see Table 4.1)

This model can be easily tweaked to account for the 'transient' switching on of the pulse. Instead of having a square temporal pulse profile, there is a finite time that the pulse takes to reach maximum intensity after turning on. The actual pulse was modelled

using a sigmoid function,

$$I(t) = \frac{c}{1 + e^{-a(t-b)}}$$

where a, b, c are fit parameters, and a polynomial function. The polynomial fit accounts for the tiny rise near 0μs.

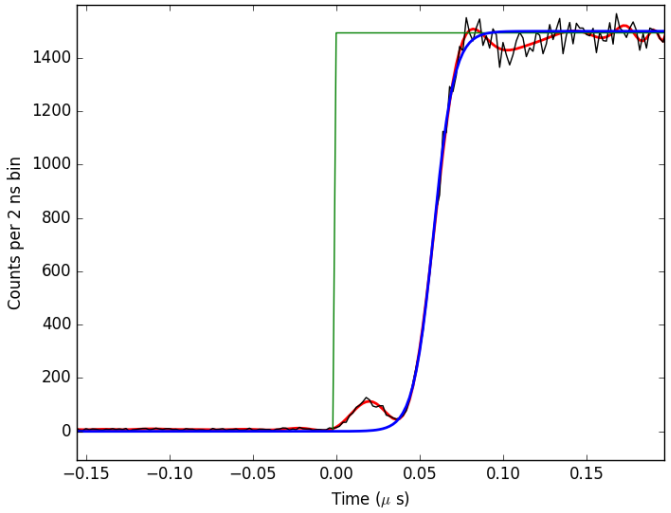

Figure 4.5: (black) Actual pulse profile, (red) polynomial fit to the actual pulse, (blue) sigmoid fit, (green) ideal pulse

As seen in Fig 4.5, both sigmoid (blue line) and polynomial fits (red line) are sufficient to describe the actual pulse. Since the intensity is no longer constant, the scattering rate from $D_{3/2}$ to $P_{1/2}$ is now time dependent, i.e. $R \to R(t)$. $R(t)$ is determined by a intensity dependent scaling of R

$$R(t) = \frac{I(t)}{I_0} \times \frac{1}{\tau(1-p)}$$

where I_0 is the maximum intensity of the pulse. Likewise, we can replace R with $R(t)$ in the rate equations (Eqn (4.3)). Similar to the ideal pulse case, we calculate the $\lambda(t)$ of red photons arriving, determine the deadtime corrected rate $\lambda_c(t)$, and finally the corrected red counts and the new branching ratio estimate. Fixing $\tau_d = 28.5$ ns, we compute the shifts $p - \bar{p}$ in the ideal and actual pulse profiles for all the pumping times used in our experiments. (see Table 4.1) It turns out that there is at most a 5% difference due to the effect of the transient switching times.

τ (μs)	Ideal [-4]	Sigmoid [-4]	Poly[-4]	Difference [%]
0.140	1.8203	1.7409	1.7822	4.5592
0.180	1.4388	1.3897	1.4162	3.5376
0.195	1.3336	1.2924	1.3144	3.1845
0.210	1.2428	1.2073	1.2260	2.9400
0.255	1.0327	1.0086	1.0205	2.3834
0.283	0.9342	0.9146	0.9238	2.1345
0.286	0.9245	0.9060	0.9143	2.0378
0.300	0.8831	0.8661	0.8734	1.9524
0.307	0.8638	0.8473	0.8542	1.9257

Table 4.1: Tabulated branching ratio shifts $p - \bar{p}$ for various pumping times, using the ideal, sigmoid and polynomial pulse profiles The percentage difference between the ideal shift and sigmoid shift is computed in the rightmost column.

4.3.2 Master equation population dynamics with rate correction

This method maintains the same rate correction method (see Eqn (4.5)), but improves on the previous model by having a quantum treatment of the population dynamics. In short, we will solve the quantum master equation for the population dynamics of $S_{1/2}, P_{1/2}, D_{3/2}$ in response to a 650 nm coupling field.

A brief discussion on basic quantum theory is necessary. For a system interacting with the environment,

$$\dot{\rho}_{tot} = -i[H_{tot}, \rho_{tot}(t)]; \quad H_{tot} = H_{sys} + H_{env} + H_{int}$$

Since we are only interested in dynamics of the system, we perform a partial trace over the environmental degrees of freedom and obtain a master equation for the motion of the system density matrix, $\rho = \mathrm{Tr}_{env}[\rho_{tot}]$. The result is the Lindblad master equation

$$\begin{aligned}\dot{\rho}(t) &= -i[H(t), \rho(t)] + \sum_n \frac{1}{2}[2C_n\rho(t)C_n^\dagger - \rho(t)C_n^\dagger C_n - C_n^\dagger C_n\rho(t)] \\ &= -i[H(t), \rho(t)] + \sum_n \frac{\gamma_n}{2}[2A_n\rho(t)A_n^\dagger - \rho(t)A_n^\dagger A_n - A_n^\dagger A_n\rho(t)]\end{aligned}$$

where $C_n = \sqrt{\gamma_n}A_n$, A_n are the operators through which environment couples to system in H_{int} and γ_n are the corresponding rates.

In our case, we perform the summation over two parameters, λ: polarisation of field that couples a transition and a: blue ($P_{1/2} \to S_{1/2}$) and red ($P_{1/2} \to D_{3/2}$) decay paths. The operator $A_{a,\lambda}$ is the dipole operator for a transition characterised by λ, a with Clebsch Gordan coefficients as its elements. The rates γ_a are the decay rates for

the red and blue decay paths, i.e. $\gamma_r = p\Gamma, \gamma_b = (1-p)\Gamma$. So we write,

$$\frac{\mathrm{d}\rho}{\mathrm{d}t} = -i[H,\rho] + \sum_{\lambda,a} \frac{\gamma_a}{2}(2A_{a,\lambda}\rho A^\dagger_{a,\lambda} - A^\dagger_{a,\lambda}A_{a,\lambda}\rho - \rho A^\dagger_{a,\lambda}A_{a,\lambda} \tag{4.6}$$

The Hamiltonian here consists of

$$H = H_{det} + H_z + H_c$$

H_{det} is the detuning that couples the ground states in the transition we are driving, i.e. $H_{det} = \Delta \sum_g |g\rangle\langle g|$. The Zeeman Hamiltonian is $H_z = g_J \mu_B m_J B_z$, where the Lande g-factors for $S_{1/2}, P_{1/2}, D_{3/2}$ are $2, \frac{2}{3}, \frac{4}{5}$. As a convention, we keep our quantisation axis pointed along the direction of the magnetic field, so H_z is always diagonal. H_c describes the coupling between states driven by the field with the key components, $\frac{\Omega_0}{2} \times$ pol $\times$ CG, where CG is a Clebsch Gordan coefficient, pol is the relevant component of light polarisation and Ω_0 is coupling strength between the 650 nm laser and the transition.

There are four quantities that determine the simulation dynamics from the master equation, (i) magnetic field strength, (ii) coupling strength of the 650 nm laser (which determines the pumping time), (iii) 650 nm light polarisation and (iv) temporal profile of the 650 nm pulse. The magnetic field strength is user specified and since we align the quantisation axis with the field direction, the magnetic field strength comes in as a constant, B_z, in H_z. The pumping times measured in the experiment determine the how fast the ion is pumped out of $D_{3/2}$ into $S_{1/2}$. We set up Ω_0 (coupling strength) in the Hamiltonian as a free parameter in our simulation, and choose a value that gives a decay behaviour of $D_{3/2}$ that agrees with the pumping time measured in an independent experiment. Figure 4.6 gives an example of the model generated population dynamics of $D_{3/2}$ from a well-selected Ω_0 matching the exponential decay of $D_{3/2}$ with characteristic time scale equal to the pumping time. Next, the 650 nm light polarisation and propagation direction are user specified. With respect to the quantisation axis, we can determine the spherical components of the polarisation. Finally, the temporal profile of the pulse is treated as a square profile here in light of the fact that the transients are expected to have a small effect ($\sim 5\%$) as seen in the previous model (see Section 4.3.1).

Once the above 4 quantities are specified, and using the best known estimate of $p = 0.268, q = 0.0268$, we can fully describe the system that starts in $D_{3/2}$ (distributed evenly in each m state) and solve how the population evolves over time. The excited

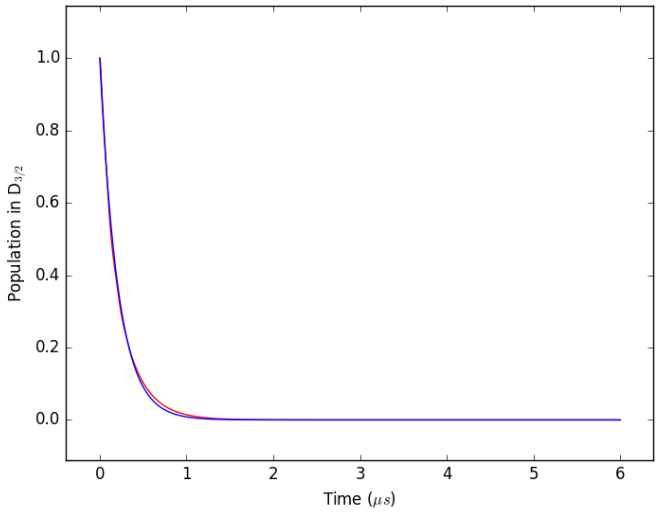

Figure 4.6: (blue) Exponential decay of $D_{3/2}$ with characteristic time scale equal to the experimentally measured pumping time. (red) Population dynamics of $D_{3/2}$ state simulated by master equation.

state ($P_{1/2}$) population can be written as the expectation value of the excited population

$$e(t) = \mathrm{Tr}\left(\sum_m \left|P_{1/2}, m\right\rangle \left\langle P_{1/2}, m\right| \rho(t)\right) \tag{4.7}$$

where the excited state projection operator is $\sum_m \left|P_{1/2}, m\right\rangle \left\langle P_{1/2}, m\right|$. The rate of 650 nm photons detected is then

$$\lambda(t) = pq\Gamma e(t)$$

Now, using $\lambda(t)$ from the simulations, we apply the rate correction (Eqn (4.5)) to find the corrected red counts and the new branching ratio estimate $\bar{p}$.

4.3.3 Master equation population dynamics with analytic count correction

This model uses the same master equation population dynamics as the previous model, but it considers a more sophisticated deadtime correction to the red counts. Instead of a simple rescaling of the rates (see Eqn (4.5)), we use the probability distribution of photon emission times $P(t)$ to examine the probabilities of subsequent photons arriving within the deadtime.

To get $P(t)$, we solve the following master equation,

$$\dot{\rho}(t) = -i[H(t), \rho(t)] - \sum_{a,\lambda} \frac{\gamma_a}{2}(A^\dagger_{a,\lambda} A_{a,\lambda}\rho + \rho A^\dagger_{a,\lambda} A_{a,\lambda}) \tag{4.8}$$

This differs from the full master equation Eqn 4.6) by the term $\sum_{a,\lambda} \gamma_\alpha A_{a,\lambda} \rho A_{a,\lambda}^\dagger$ because we are not interested in knowing ground state population dynamics. Instead, we want to know the time statistics of decay of the excited state. Similar to the previous, we still specify the magnetic field, 650 nm polarisation, pumping times and assume a constant pulse in the simulation. Upon solving for $\rho(t)$, $P(t)$ can be obtained via

$$P(t) = \Gamma \operatorname{Tr}\left(\sum_m \left| P_{1/2}, m \right\rangle \left\langle P_{1/2}, m \right| \rho(t) \right) \tag{4.9}$$

and $P(t)$ obeys the normalisation condition

$$\int_{\text{pulse}} P(t) dt = 1$$

We proceed with the description of our model. For the best estimated $p = 0.268, q = 0.0268$, the distribution for k detected photons when pumping the ion from $D_{3/2}$ to $S_{1/2}$ by a deadtime free detector is $f(k; p, q)$ (see Eqn (3.6)). With deadtime, the distribution function for k photons will definitely change and it would be difficult to determine this new distribution. Instead, one can keep $f(k; p, q)$ unchanged but assign $f(k; p, q)$ as the probability of detecting some effective number of photons which is $< k$.The corrected r is

$$r = \sum_k f(k; p, q) \bar{k}_k \tag{4.10}$$

where $\bar{k}_k$ is the effective counts given k counts in the ideal case. Once the $\bar{k}_k$ and the corrected r is determined, we can compute the new branching ratio estimate $\bar{p}$ using Eqn (3.3).

We will now demonstrate how to determine $\bar{k}_k$ by using the probability distribution of photon emission times $P(t)$. First, we define the recursive functions

$$P_m(t) = \int_0^t P_{m-1}(t - x) P_0(x) dx; \qquad P_0(t) = P(t) \tag{4.11}$$

where $P_m(t)$ is the arrival time probability distribution of a subsequent detected photon, given that m photons were missed. The probability of the subsequent detected photon arriving within the deadtime, given m photons were missed, is

$$p_m = \int_0^{\tau_d} P_m(t) dt \tag{4.12}$$

$\mathbf{k = 2}$ **case**: First consider $n = 2$ photons emitted and $k = 2$ photons reaching the detector. The detector detects one count if the second arrives within τ_d of the first. So,

the probability of one count instead of two is

$$p_0 = \int_0^{\tau_d} P(t)dt \tag{4.13}$$

There may be $n = 3$ photons emitted and $k = 2$ detected photons as well. There are 3 possible configurations in this case, $(1,1,0),(0,1,1),(1,0,1)$, where "1" indicates a count, "0" otherwise. For the first two configurations, the probability of getting one count is in Eqn (4.13). In the last configuration, there is one missed photon between the two detected photons. The distribution arrival time of the third photon is

$$P_1(t) = \int_0^t P(t-t_2)P(t_2)dt_2$$

So, in (1,0,1), the probability of getting the third photon within the dead-time of the first detected photon is

$$p_1 = \int_0^{\tau_d} P_1(t)dt = \int_0^{\tau_d} \left[\int_0^t P(t-x)P(x)dx\right] dt \tag{4.14}$$

If there are $n = 4$ photons emitted and $k = 2$ photons detected, this gives 6 configurations: (1,1,0,0), (0,1,1,0), (0,0,1,1), (1,0,1,0), (0,1,0,1), (1,0,0,1). The probability of getting one count for the first 3 configurations is described by Eqn (4.13). The probability of getting one counts for the fourth and fifth configurations is described by Eqn (4.14). The last (1,0,0,1) configuration involves two missed photons. The probability distribution for arrival of the fourth photon given two were missed is

$$P_2(t) = \int_0^t P(t-t_3)\int_0^{t_3} P(t_3-t_2)P(t_2)dt_2dt_3$$

So, in (1,0,0,1), the probability of getting one count is

$$\begin{aligned} p_2 &= \int_0^{\tau_d} P_2(t)dt \\ &= \int_0^{\tau_d} \left[\int_0^t P(t-t_3)\int_0^{t_3} P(t_3-t_2)P(t_2)dt_2dt_3\right] dt \end{aligned} \tag{4.15}$$

So, for arbitrary $n \geq 2$, $k = 2$, one can repeat this to find the net probability of getting one count instead of two due to τ_d.

$$\begin{aligned} &\sum_{n=m+2}^{\infty}\sum_{m=0}^{n-2}[p^n(1-p)][{}^nC_2q^2(1-q)^{n-2}]\left[\frac{n-(m+1)}{{}^nC_2}p_m\right] \\ &= (1-p(1-q))f(2;p,q)\sum_m p^m(1-q)^m p_m \end{aligned}$$

where ${}^nC_2 = \binom{n}{2}$. The first term in parenthesis describes the probability of obtaining n

emitted photons from geometric distribution. The second term in parenthesis describes the probability of getting 2 detected photons out of n emitted photons. The third term in parenthesis states that the number of ways two photons can arrive with m missing photons in between is $n-m-1$ out of ${}^nC_2$. The effective mean count for $k=2$ is

$$\bar{k}_2 = 2 - (1 - p(1-q)) \sum_m p^m (1-q)^m p_m \tag{4.16}$$

$\bar{k}_2$ has a summation over m (number of missed photons between two hits). But, in our experiments, the probability of getting 4 photons is 10^{-8}. Thus it is reasonable to sum till $m=2$.

$\mathbf{k=3}$ case: Consider $n=3$ photons emitted and $k=3$ photons reaching the detector. With dead-time, this can give 1,2 or 3 counts. Consider the extreme case where the second and third arrives within τ_d of the first. The probability of having one count out of possible 3

$$p_{3,1} = \int_0^{\tau_d} \int_0^{\tau_d - t_3} P(t_3) P(t_2) dt_2 dt_3 \tag{4.17}$$

The other extreme case is that all 3 photons are separated by at least τ_d. The probability of getting 3 counts out of 3 is

$$p_{3,3} = \left(1 - \int_0^{\tau_d} P(t) dt\right)^2 \tag{4.18}$$

Thus by normalisation, the probability of getting 2 counts out of 3 is $1 - p_{3,1} - p_{3,2}$ (the combined probability of getting 1,2,3 counts of a possible 3 is unity). There are also $n > 3, k = 3$ cases to consider. But it gets really complicated from here due to the diverse combinations. We are warranted in excluding these cases with $n > 3$ photons because of the low probability of getting $n > 3$ photons in our experiments. Instead, we can establish a lower bound and upper bound $\bar{k}_3$,

$$\sum_{i=1}^{3} i \times p_{3i} < \bar{k}_3 < 3$$

We chose our estimation of $\bar{k}_3$ as the midpoint between the lower and upper bound

$$\bar{k}_3 = \frac{1}{2}\left(3 + \sum_i^3 i \times p_{3i}\right) \tag{4.19}$$

And the error in this estimate half the difference between the upper and lower bound, $\frac{1}{2}(3 - \sum_i i \times p_{3i})$.

With $\bar{k}_2, \bar{k}_3$ established, using a best known estimate of $p = 0.268, q = 0.0268$, $\tau_d = 28.5$ ns, we calculated the shifts for the various pumping times and magnetic

field configurations used in the experiment. From our simulation results, the error in estimating $\bar{k}_3$ is only about $1-2\%$ so this validates our use of Eqn (4.19).

4.3.4 Summary

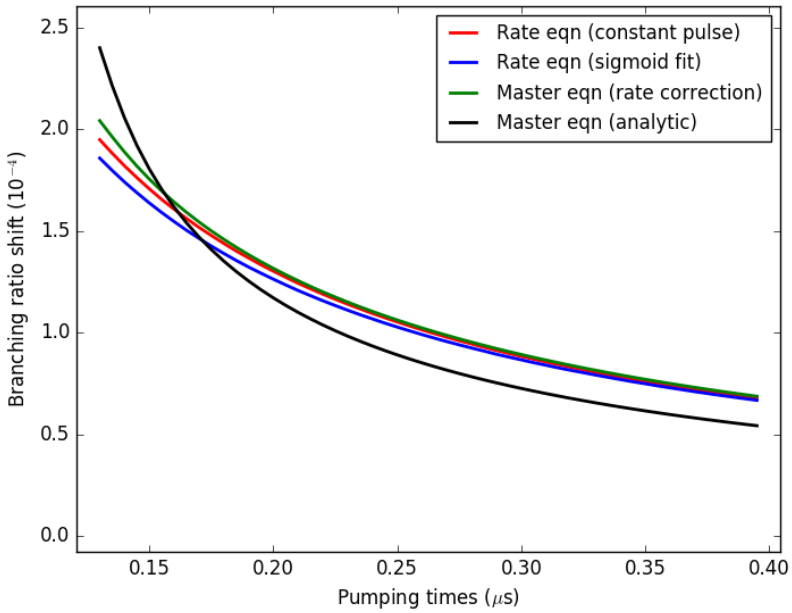

Figure 4.7: Shifts, $p-\bar{p}$, against pumping time generated by the 3 different models. (red) Rate equation model considering constant pulse, (blue) rate equation model considering pulse transients, (green) master equation model with rate correction, (black) master equation model with analytic count correction.

To summarise, we are focused on deadtime effects on the red photon counts when pumping from $D_{3/2}$ to $S_{1/2}$. We used 3 models to determine this. The first uses the rate equations to simulate dynamics and implements a rate correction for deadtime. The second uses master equation population dynamics with the same rate correction. The third uses master equation dynamics to evaluate an analytic correction accounting for the proper proper distribution of emission times.

We used these models to have a preliminary assessment of the shifts associated with deadtime. We fix the magnetic field to a typical value of 2.23 G and vary the pumping times over the range used in our experiments. From Figure 4.7, we note the following observations

1. Generally, the shifts predicted by the models vary in a consistent way. As the pumping times get longer, there is lower probability of photons coming in within the deadtime, thus the shifts decrease across all models.

2. The rate equation models (blue and green lines) and the master equation with rate correction model (red line) tend to agree as the pumping times get larger.

This is because for longer pump times, the master equation dynamics are well approximated by the rate equation dynamics. Conversely, the difference between the models will be apparent if we make the pumping times really short. For example, Figure 4.8 shows the true dynamics (blue line) obtained from the master equation for a short pumping time (30 ns) compared to the rate equation model which is not a valid physical model in this regime.

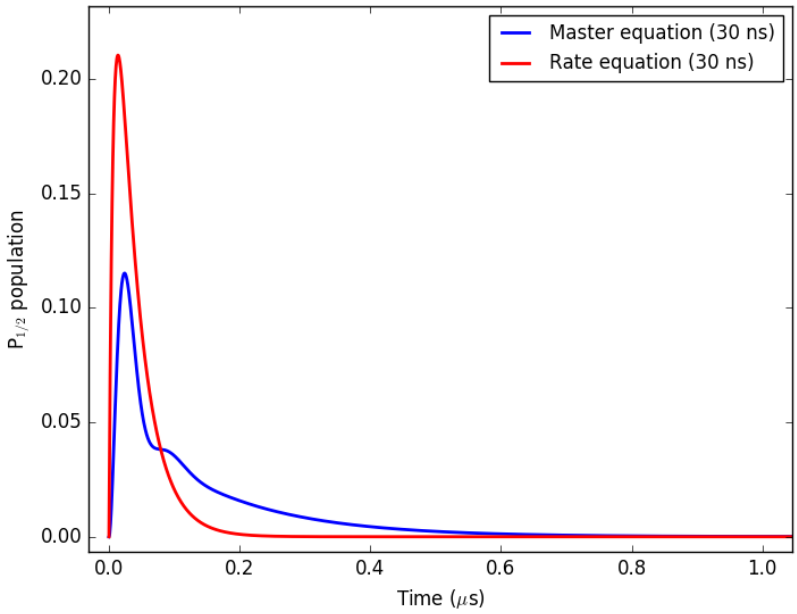

Figure 4.8: $P_{1/2}$ population with time generated using master equation (blue line) and rate equation (green line) using a short pumping time of 30 ns.

3. In Figure 4.7, the shifts from the master equation using analytic corrections (black line) undershoots the other models that use rate corrections (red, blue, green line) at longer pump times and overshoots at shorter pump times. Implicit in the rate corrections is the fact that photon arrival times are governed by a exponential distribution, $P(t) = \lambda(t)e^{-\lambda(t)t}$. In contrast, the $P(t)$ from the master equation fully accounts for the quantum nature of single atom emissions (atom cannot emit photon until it is excited). With reference to Figure 4.9, at short pumping times (100 ns), the $P(t)$ of the master equation (blue) has a higher peak in the deadtime region than the $P(t)$ of the rate equation (red). Thus, the probability of photons arriving within the deadtime is relatively higher resulting in greater computed shifts. At longer pumping times (400 ns), the $P(t)$ from the master equation (green) has a slower rise time than the $P(t)$ from the rate equation (black), resulting in lower probability of photon falling within the deadtime.

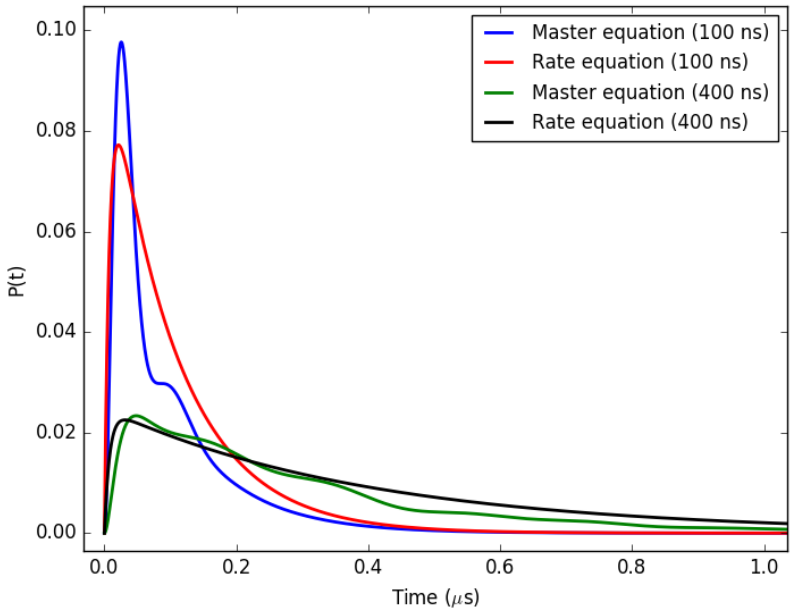

Figure 4.9: Photon arrival time distributions, $P(t)$, generated from master equation and rate equation, with different pumping times.

4.3.5 Supplementary: Validation of master equation model

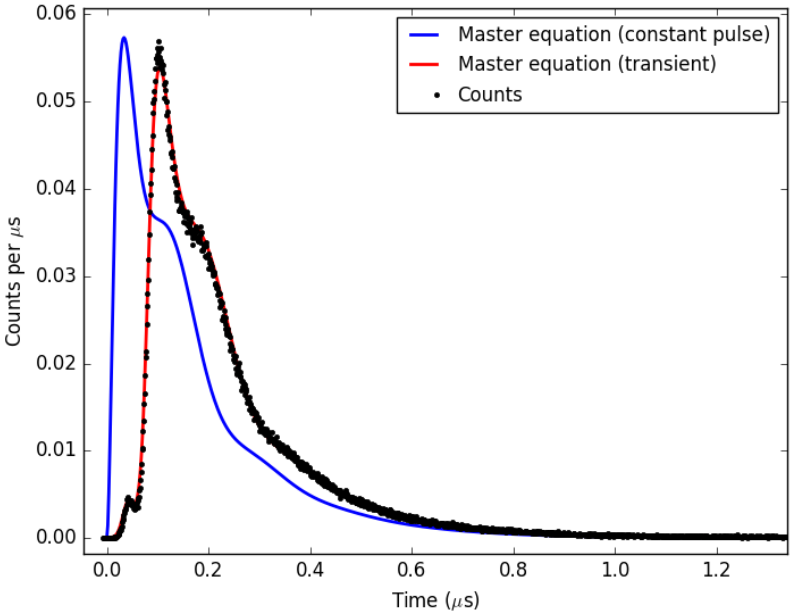

Figure 4.10: (black) Red photons collected when pumping from $D_{3/2}$ to $S_{1/2}$, with a 2.23 G magnetic field, 150 ns pumping time, 650 nm perpendicularly polarised, using high resolution time tagging. Under the same conditions, we compute the rate of red photon emissions (see Eqn (4.7)) using a constant pulse (blue) and considering the pulse transient (red).

In the above models that utilise the master equations, we specify the pumping time,

magnetic field, 650 nm polarisations to solve for the population dynamics, and use them to compute the branching ratio shifts. We will show here that the master equation we constructed (see Eqn (4.6)) indeed simulates our system well. We conducted independent experiments with a high resolution time tagger for a chosen magnetic field configration, light polarisation and pumping time. With reference to Figure 4.10, the black dots refers to the photons collected when pumping from $D_{3/2}$ to $P_{1/2}$. The blue line is $\lambda(t)$ obtained via the master equation. It is clear that even with a constant pulse, the population dynamics are sufficiently well modelled by our master equation model. If one accounts for the pulse transients, there is a remarkable fit between the master equation result (red line) and the experimental counts, with no free parameters needed. This is a validation that the master equation dynamics produced in our simulation is indeed reflected in our experiments. Furthermore, our knowledge of the magnetic field, pumping time and 650 nm polarisations was sufficient to characterise any given experiment.

4.3.6 Supplementary: Numerical experiments

As an additional consistency check for our rate and master equation models, we performed numerical simulations of the branching ratio shifts. First, we randomly sample N numbers, n, from a geometric distribution characterised by the best known branching ratio estimate p. This is equivalent to pumping the atom from $D_{3/2}$ to $S_{1/2}$ N times and getting the red photon emissions, n, from each experiment. Next, from solving the master equation (see Eqn (4.6)), we obtain the photon emission time statistics, $P(t)$, and we assign an emission time to each photon. Then, each photon is selected via a Bernoulli trial with probability $q = 0.0268$, replicating the detection process. The mean of these counts should be $\sim \frac{qp}{1-p}$. To implement a deadtime correction, we check for the time difference between neighbouring photons from each experiment. If the subsequent photon arrives within the deadtime of a detected photon, this photon is removed from the photon counts of that experiment. The mean corrected red photon counts is fed to Eqn (3.3) to determine the new $\bar{p}$. Preliminary runs yielded shifts that were consistent with the four models.

Chapter 5

Other systematics

We have also explored other systematics cited in literature but these were determined to be negligible at the level of accuracy we are concerned with. In this chapter, we offer a description of these systematics and our analysis of their effect.

5.1 Finite lifetime of $D_{3/2}$

During optical pumping from $S_{1/2}$ to $D_{3/2}$, there is a small probability that the ion may decay from $D_{3/2}$ back to $S_{1/2}$ resulting in an increase in the signal. The optical pumping from $S_{1/2}$ to $D_{3/2}$ can be described as an exponential with time scale τ_b. Denoting γ as the decay rate of $D_{3/2}$, T as the length of the pulse, the probability of decay of $D_{3/2}$ is simply the decay rate multiplied with the population of the $D_{3/2}$ state.

$$\gamma \int_0^T 1 - e^{-t/\tau_b} dt \approx \gamma(T - \tau_b)$$

For a detection efficiency, q, the counts collected in the first 493 nm pulse is

$$q + q\gamma(T - \tau_b) + \text{background}$$

and the counts collected during the second 493 nm pulse is

$$q\gamma T + \text{background}$$

Upon performing background subtraction, we get

$$q(1 - \gamma\tau_b)$$

Hence, the above represents a fractional decrease in background subtracted signal of $-\gamma\tau_b$.

The lifetime of the $D_{3/2}$ level also affects optical pumping from $D_{3/2}$ to $S_{1/2}$. In this

case, the background is not affected because the $D_{3/2}$ is only transiently occupied. This gives a decay probability of approximately $-\gamma\tau_r$, which is the fractional decrease in the measured signal. For Ba^+, the $\gamma_{r,b} \sim 0.0125/\text{s}$, and $\gamma\tau < 5 \times 10^{-9}$. Thus the effect is negligible.

5.2 Off resonant excitation to $P_{3/2}$

During optical pumping from $S_{1/2}$ to $D_{3/2}$, there is a small probability of off-resonant excitation to $P_{3/2}$. In this event, the atom can scatter to $S_{1/2}$, $D_{3/2}$ or $D_{5/2}$ with probability $p_{1/2}$, $p_{3/2}$ and $p_{5/2}$ respectively. Scattering to $D_{5/2}$ places the ion in a dark state, and this will be known during the cooling pulse with 493 and 650 nm beams since the ion won't fluoresce. If the atom scatters back to $S_{1/2}$, the pumping will still continue and there is no effect on the b signal. Thus the issue occurs only when it scatters to $D_{3/2}$ and the emitted photon (<650 nm) is not detected. The probability of scattering from $P_{3/2}$ to $D_{3/2}$ is

$$p_{3/2}\Gamma\frac{\Omega_b^2}{4\Delta^2}\tau_b$$

where Γ is the linewidth of $P_{3/2}$, Ω_b is the coupling strength to the 493 nm laser to $P_{3/2}$ level, Δ is approximately the fine structure splitting between $P_{3/2}$ and $P_{1/2}$ and τ_b is the pumping time for the 493 nm beam. This also represents the fractional decrease in the b signal. The same analysis can be repeated when pumping from $D_{3/2}$ back to $S_{1/2}$. Here, the problem occurs when the ion scatters to $S_{1/2}$ and no red photons are emitted. The fractional decrease in the r signal is

$$p_{1/2}\Gamma\frac{\Omega_r^2}{4\Delta^2}\tau_r$$

where Ω_r is the coupling strength between 650 nm laser and the $P_{3/2}$ level, τ_r is the pumping time for the 650 nm beam, the Γ, Δ definitions follow from the previous case. In our experiments, the pumping times are short ($\tau_{r,b} \leq 300$ ns) and the fine structure splitting is large ($\Delta = 2\pi \times 50.7$THz). Thus, the fractional change is negligible.

5.3 Finite pulse duration

The finite duration of the pulses can result in either a loss of accuracy or precision. If the pulses are too long, it will take too much time to accumulate enough data to reach a desired level of precision. If the duration is too short, there will be incomplete transfer of population affecting the accuracy of the branching ratio estimate. In our experiments, we kept the duration of the laser pulses to be at least 20τ where τ (pumping time)

is the independently measured characteristic time scale to pump $S_{1/2} \leftrightarrow D_{3/2}$ using 493 and 650 nm lasers. This ensures that the population left behind is negligibly small $e^{-20} \sim 10^{-9}$ while at the same time not needing to collect data for overly long periods.

Chapter 6

Conclusion

In conclusion, this work was part of a bigger effort to characterise the dynamic differential scalar polarisability, $\Delta\alpha_0(\omega)$ of a Barium clock transition, which in turn enables Barium to provide accurate calibration of the environment. The research group did earlier work that showed $\Delta\alpha_0(\omega)$ in Barium can be largely specified using measured matrix elements (associated with three dominant contributions). All other contributions can be modelled by a single UV pole that basically offsets the curve, and this can be constrained by finding the zero crossing. We have also shown that each matrix element can be determined by experimental measurements, one of them is the branching ratio associated with the states in the matrix element. My project was focused on confirming measurement claims of the $P_{1/2} \rightarrow D_{3/2}$ branching ratio that was made in the literature.

We have presented our raw data from 16 measurements of the branching ratio, over a course of 6 months. We identified two key systematics, and one of them (detector deadtime) was extensively modelled in this report. We tested various models to assess the deadtime effect and for sufficiently slow pumping times, the models that use rate correction show reasonable agreement ($\sim 10\%$) with the model accounting for the quantum dynamics of photon emission. For the pumping times used in our experiment, preliminary results indicate that the shifts to our measured values are $\sim 1 \times 10^{-4}$.

While this report has showcased the preliminary assessment for a deadtime correction to the branching ratio estimate, further work is needed in determining the shifts associated with the second key systematic identified, imperfect background subtraction (see section 3.2.2).

Chapter 7

Appendix

7.1 Deadtime corrected photon Poisson counting distribution

The rate corrections (see Eqn (4.5)) implemented follows from [7]. In the absence of deadtime, the probability of recording n counts in a time interval T in a detector illuminated by a laser source is

$$p(n,\lambda) = \frac{(\lambda T)^n e^{-\lambda T}}{n!}$$

where $\lambda = \alpha I$, α is the quantum efficiency of the detector and I is the irradiance at the detector. In the presence of deadtime, τ_d, the probability of registering n counts in a time interval T is given exactly by

$$\begin{aligned} p_0(n,\lambda,\tau_d) = &\sum_{k=0}^{n} \left[\frac{\lambda^k (T - n\tau_d)^k}{k!}\right] e^{-\lambda(T-n\tau_d)} \\ &- \sum_{k=0}^{n-1} \left[\frac{\lambda^k (T - (n-1)\tau_d)^k}{k!}\right] e^{-\lambda(T-(n-1)\tau_d)} \end{aligned}$$

The above expression is valid for counts n such that $n\tau_d < T$. The new mean of this distribution $\bar{n}$ to first order is

$$\bar{n} = \frac{\lambda T}{1 + \lambda\tau_d}$$

This is exactly the rate corrections we implemented in 3 of the models.

Bibliography

[1] Poli, N., Oates, C., Gill, P., Tino, G. (2014). Optical atomic clocks. *arXiv e-prints*. arXiv: 1401.2378

[2] Ludlow, A., Boyd, M., Ye, J.,Peik, E. (2015). Optical atomic clocks. *Rev. Mod. Phys*, 87(2), 637-701.

[3] Arnold, K., Kaewuam, R.,Roy, A., Tan, T.R., Barrett, M.D. (2018) Blackbody radiation shift assessment for a Lutetium ion clock. *Nature Communications*, 9(1650).

[4] Angel, J., Sandars, P. (1968). The hyperfine structure Stark effect I. Theory. *Proceedings of the Royal Society of London*, 305(1480).

[5] Stipcevic, M., Christensen, B., Kwait, P., Gauthier, D. (2017). Advanced active quenching circuit for ultra-fast quantum cryptography. *Optics Express*, 25(18), 21861-21876.

[6] Giuseppe, A.D. (2013). *Metrology and Physical Constants*. IOS Press.

[7] Cantor, B., Teich, M. (1974) Dead-time-corrected photocounting distributions for laser radiation. *Journal of the optical society of America*, 65(7), 768-791.